Journal of Engineering Physics and Thermophysics, Vol. 74, No. 6, 2001

STUDY OF BULK AND NANOSCALE MATERIALS BY TIGHT-BINDING AND PATH PROBABILITY METHODS

K. Masuda-Jindo,[a] R. Kikuchi,[b] and M. Menon[c]

UDC 531.4:541.1:519.21

The generalized tight-binding molecular dynamics (TBMD) method is used to study the atomistic and mechanical properties of the nanoscale materials and the calculated properties are compared with those of the corresponding bulk materials. We report that the thermodynamic and mechanical properties of the nanoscale materials are quite different from those of the corresponding bulk materials. For instance, it has been found that the excess energies of dislocations in the small crystallites are very small and often take negative values due to the atomistic "image effects". The edge dislocation in the carbon nanotubes, whose core is characterized by a pentagon-heptagon pair is found to act as a center of the stress concentration and contribute to the peculiar nanoplasticity in the quasi-one-dimensional (1D) cylindrical structures. Using the path probability method (PPM) in the statistical physics, we also study the growth and microstructure of strained SiGe deposited films on Si(001) substrate, taking into account the composition gradient and influence of the strain filed at the heterojunction.

1. INTRODUCTION

Recently, there has been a great interest in the study of nanoscale materials since they provide us a wide variety of academic problems as well as the technological applications [1–12]. In particular, the important experimental findings in this field are the discovery of carbon nanotubes and the discovery of superconductivity in the alkali-metal doped C_{60} system. The properties of clusters and fine particles are generally quite different from those of the bulk materials, e.g., in magnetism, catalytic activities, elastic properties, and optical properties. The discovery of carbon nanotubes (CNT) by Iijima [3] and subsequent observations of CNT's unique mechanical and electronic properties have initiated intensive research on these quasi-one-dimensional structures. CNT's have been identified as one of the most promising building blocks for future development of functional nanostructures. One of the purposes of the present paper is to investigate the plasticity of materials with quasi-1D structures using the quantum generalized tight-binding molecular dynamics (GTBMD) scheme of Menon and Subbaswamy [8–11]. In addition, we also calculate the atomic configurations and electronic states of C and Si clusters including extended defects (dislocations and/or grain boundaries) [13] and compare the mechanical properties of the nanoscale crystallites with those of bulk materials.

In the second part of the present study, we investigate the junction relaxation processes of semiconductor heterostructures like SiGe/Si(001) [14–19] and ZnSe/GaAs(001) systems [20–22]. The thermodynamic stabilities of the semiconductor heterostructures will be investigated by using the tight-binding (TB) orbital

[a]Department of Materials Science and Engineering, Tokyo Institute of Technology, Nagatsuta, Midori-ku, Yokohama 226-8503, Japan; email: kmjindo@issp.u-tokyo.ac.jp; [b]Materials Science and Mineral Engineering, University of California, Berkeley, CA 94720-1760, USA; [c]Department of Physics and Astronomy, University of Kentucky, Lexington, Kentucky 40506, USA. Original article submitted December 19, 2000.

 1062-0125/01/7406-1484$25.00 ©2001 Plenum Publishing Corporation

peeling method and the path probability method in the statistical physics [23–25]. It will be shown that the junction relaxation exhibits the characteristic features, e.g., overshooting and uphill diffusion along the chemical potential gradient depending on the temperature and relative magnitude of the effective pair interaction energies.

2. PRINCIPLE OF CALCULATIONS

2a. TBMD Method. For performing the molecular dynamics simulations, we use the total energy calculation procedure based on the TB electronic theory. The total energy of the system is assumed to be given by a sum of two terms [8–11]:

$$U = U_{\mathrm{el}} + U_{\mathrm{rep}} = \sum_k \varepsilon_k + (1/2) \sum_{ij} \phi(r_{ij}) , \tag{1}$$

where U_{el} is the band structure energies ε_k for the occupied states and U_{rep} represents the remaining repulsive energy contribution. Here r_{ij} is the separation of atoms i and j. The repulsive potential $\phi(r)$ is taken to be short ranged and varies exponentially with the interatomic distance. For treating the nanoscale semiconductor crystallites, we will use the minimal parameter generalized tight-binding molecular dynamics scheme of nonorthogonal basis [8–11]. For the GTB scheme, the characteristic equation to be solved is written in a matrix form as

$$(\mathbf{H} - \mathbf{E}_n\mathbf{S})\, \mathbf{C}^n = 0 , \tag{2}$$

where $\mathbf{H}$ and $\mathbf{S}$ are the Hamiltonian and overlap matrixes, respectively and $\mathbf{C}^n$ is the column vector of LCAO coefficients. Evaluation of (2) is expedited by the use of the Cholesky factorization in which the overlap matrix $\mathbf{S}$ is factored into $\mathbf{S} = \mathbf{B}\mathbf{B}^+$. This factorization is always possible provided $\mathbf{S}$ is positive definite. The method has been found to be very reliable in obtaining good agreement with experimental results for the structural and vibrational properties of fullerenes and nanotubes [8–11].

Furthermore, for treating the large-scale systems containing more than 1000 atoms, we will use the nonorthogonal density matrix (DM) scheme [26]. The DM in a nonorthogonal basis is introduced by defining the two quantities

$$\overline{X} = S^{-1}\, X\, S^{-1} , \quad \overline{\rho} = 3\overline{X}S\overline{X} - 2\overline{X}S\overline{X}S\overline{X} \tag{3}$$

as alternative representation for the trial and physical DM, respectively. In terms of $\overline{X}$ and $\overline{\rho}$ the particle (electron) number becomes

$$N_{\mathrm{el}} = \mathrm{Tr}\, [(3\overline{X}S\overline{X} - 2\overline{X}S\overline{X}S\overline{X})\, S] , \tag{4}$$

and the energy functional is written as

$$\Omega = \mathrm{Tr}\, [(3\overline{X}S\overline{X} - 2\overline{X}S\overline{X}S\overline{X})\, H'] . \tag{5}$$

In order to achieve linear scaling, a cutoff radius (R_{c}) is postulated beyond which all elements of the trial density matrix are set to zero. This leads to a sparse density matrix, which gives linear scaling.

The present TB theory involves the following six parameters for elemental semiconductors: the diagonal matrix elements (atomic term values) ε_s and ε_p; the covalent radius ($d_0/2$); the interaction fall off rate α; the nonorthogonality constant K; and the repulsive coefficient χ_0. Of these, ε_s, ε_p, and d_0 are set a priori from Harrison's work, and are not adjusted. The four two-center hopping integrals $V_{\lambda\lambda'\mu}$ are derived from the di-

mensionless universal parameters through a prescription given by Harrison, and have the values $V_{ss\sigma}$ = −2.37 eV, $V_{sp\sigma}$ = 2.52 eV, $V_{pp\sigma}$ = 3.32 eV, and $V_{pp\pi}$ = −1.07 eV for Si. Thus, in our scheme there are only three adjustable parameters, α, K, and χ_0. These can be fitted simply either to a dimer or the crystalline solid for experimental bond length and frequencies.

2b. Path Probability Method. In this subsection, we focus our attention on the relaxation process of the semiconductor heterostructures. To study the interface disorder, we use the path probability method [23–25]. The essence of PPM in the statistical physics will be outlined below. We work with a binary system with vacancies, and i = 0, 1, and 2 are used to designate a vacancy, an A atom and a B atom, respectively. We use the state variables and the path variables, which are defined as follows. The variables which specify the state of the system at time t are called the state variables, and we use point variable $x_n(i;\ t)$ and pair variable $y_v(i,\ j;\ t)$, where i and j are 0, 1 or 2, $x_n(i;\ t)$ is the probability of finding a species i at an nth lattice point at time t, whereas $y_v(i,\ j;\ t)$ is the probability of finding i at an nth point and j at an adjacent $(n+1)$th point at time t.

In the PPM procedure, the path probability function (PPF) is given in terms of the path variables, and then we maximize the PPF to derive the most probable path relations, to obtain the differential equations to describe how the system changes in time.

The PPF P is made of three factors: $P = P_1$, P_2, and P_3. P_1 is for the jump probabilities including the common activation energy contribution, P_2 is for the activation energy contribution, it depends on the initial energy level and does not depend on the final energy. P_3 is for the number of way and needs careful counting near the surface. In the following equations, N is the number of lattice points for each n plane, and $2N$ is the number of bonds for each ν position.

First, P_1 is given as

$$\ln P_1\,(t;\,t+\Delta t) = 2N \sum_i \ln\,(\Delta t\,\Theta_i) \sum^{\nu\le n_s-1} \left(Y_\nu\,(i0;\,0i)_{\rm u} + Y_\nu\,(0i;\,i0)_{\rm d}\right)\,, \tag{6}$$

where n_s denotes the topmost surface layer of the deposited film. The subscript "u" is for an upward jump of an atom, while "d" is for a downward jump of an atom.

Here it is noted that P_1 is written in terms of the exchange variables and Θ_i is defined by

$$\Theta_i \equiv \theta_i \exp\,(-\,\beta U_i)\,. \tag{7}$$

This includes the oscillation frequency θ_i, that is also called the attempt frequency, of an ith atom and the activation energy U_i, which is for an ith atom to jump into a neighboring vacancy, measured above the 0 level of the pair energy ε_{ij}.

The second factor P_2 is for the energy to be supplied from the heat bath, depending on the initial energy level. It is written as

$$P_2\,(t;\,t+\Delta t) = \exp\,(-\,\beta\Delta E_{\rm supplied})\,. \tag{8}$$

We write the energy to be supplied for breaking an i–j bond as $\varepsilon_{ij}(\nu)$ (> 0), so that

$$\Delta E_{\rm supplied} = 2N \sum_{ij} [\{ \sum^{\nu\le n_s-1} \varepsilon_{ij}\,(\nu) \left\{2Y_\nu\,(ij;\,0j)_{\rm d} + Y_\nu\,(ij;\,0j)_{\rm u} + Y_\nu\,(ij;\,i0)_{\rm d}\right\} + \\ + \sum^{\nu\le n_s-1} \varepsilon_{ij}\,(\nu)\,2Y_\nu\,(ij;\,0j)_{\rm u} \}right]\,. \tag{9}$$

In this expression, we made $\varepsilon_{ij}(\nu)$ to depend on the position of the layer. Here it is noted that the pair interaction energies ε_{ij} depend sensitively on the location of the atomic planes with respect to the interface plane, due to the existence of the mismatch strain, interface defects, and layer-dependent alloy compositions. For thin films with a larger equilibrium lattice constant than that of the substrate, like ZnSe/GaAs, GaAs/Si, and Ge_xSi_{1-x}/Si(001) systems, a tetragonal distortion occurs under biaxial compression parallel to the interface. This results in an increase of the lattice constant $a_\perp$ perpendicular to the interface $a_\perp = [1 - (2C_{12}/C_{11})\varepsilon_{xx}]a_0$, where a_0 denotes the equilibrium lattice constant of the epilayer material.

The third factor P_3 is the degeneracy number and is derived from the CVM pair expression for the coordination number 4. However, since we have the surface for treating the deposited films, we cannot use the expression for the infinite systems. We start from constructing the W factor from the correlation correction factor

$$P_3(t; t+\Delta t) = \prod^{n \le n_s} W_{pt}(n; N) \prod^{n \le n_s - 1} G_{pair}(\nu; 2N) . \tag{10}$$

Since we take the pair variable as basic, the first factor is rewritten in pairs:

$$\prod^{n \le n_s} W_{pt}(n; N) = [W_{pt}(n_s; N)]^{1/2} \prod^{n \le n_s - 1} [W_{pt}(n; N)\, W_{pt}(n+1; N)]^{1/2} . \tag{11}$$

Then (10) is rewritten as

$$P_3(t; t+\Delta t) = [W_{pt}(n_s - 1; N)]^{1/2}\, W_{pt}(n_s; N)\, G_{pair}(n_s - 1; 2N) \times$$
$$\times \prod^{\nu \le n_s - 2} \left\{[W_{pt}(n; N)\, W_{pt}(n+1; N)]^{1/2}\, G_{pair}(\nu; 2N)\right\} . \tag{12}$$

For evaluating W_{pt} and G_{pair}, we use the following relations

$$W_{pt}(n; N) \equiv \frac{N\,!}{\{\text{Point}(n)\}_N} , \tag{13a}$$

$$G_{pair}(\nu; 2N) \equiv \frac{\{\text{Point}(n)\}_{2N}\{\text{Point}(n+1)\}_{2N}}{(2N)\,!\,\{\text{Pair}(\nu)\}_{2N}} = \left(\frac{\{\text{Point}(n)\}_N\ \{\text{Point}(n+1)\}_N}{N\,!\,\{\text{Pair}(\nu)\}_N}\right)^2 \tag{13b}$$

where $\{\text{Point}(n)\}_N = \sum L(x_n(i;\ t))$ and $\{\text{Pair}(\nu)\}_N = \prod_{ij}(Ly_\nu(i,\ j;\ t)!$ with $L(x) = X \ln X - X$.

Then substituting Eq. (13) into Eq. (12) leads to

$$P_3(t; t+\Delta t) = \frac{\{\text{Point}(n_s - 1)\}_N^{3/2}\{\text{Point}(n_s)\}_N}{N\,!^{1/2}\{\text{Pair}(n_s - 1)\}_N^2} \prod^{\nu \le n_s - 2} \frac{\{\text{Point}(n)\}_N^{3/2}\{\text{Point}(n+1)\}_N^{3/2}}{N\,!\,\{\text{Pair}(\nu)\}_N^2} . \tag{14}$$

The product part corresponding to the expression for the coordination number 4 is given by

$$W\,[\text{pair}] = \frac{\{\text{Point}\}_N^3}{N\,!\,\{\text{Pair}\}_N^2}\,. \tag{15}$$

The first factor in (12) is to take care of the surface. This leads to the final result for the exchange variable $Y(0i;\ i0;\ \nu)_{\text{d}}$:

$$Y\,(0i;\,i0;\,\nu)_{\text{d}} = \Delta t\;\Theta_i\,(\nu)\;y_\nu\,(0i;\,t)\,\frac{\Lambda_\nu\,({}^*i)\;\Lambda_{\nu+1}\,(i^*)^2}{x_{n+1}\,(i;\,t)^3}\,,\quad \nu \le n_{\text{s}} - 2\,. \tag{16}$$

Using the similar transformations, we derive the result for $Y(i0;\ 0i;\ \nu)_{\text{u}}$ as

$$Y\,(i0;\,0i;\,\nu)_{\text{u}} = \Delta t\;\Theta_i\,(\nu)\;y_\nu\,(i0;\,t)\,\frac{\Lambda_{\nu-1}\,({}^*i)^2\;\Lambda_\nu\,(i^*)}{x_n\,(i;\,t)^3}\,,\quad \nu \le n_{\text{s}} - 2\,. \tag{17}$$

These relations can be understood as follows. In Eq. (16), as i on the $(n+1)$th plane jumps downward, the bonds being broken are one ν bond and two $\nu+1$ bonds. These broken bonds contribute to the Λ_ν and $\Lambda_{\nu+1}^2$ factors. The denominator is a part of the superposition relation to show that in the initial $y_\nu(0i;\ t)$ the $(n\ +\ 1)$th lattice point is occupied by i. In Eq. (17), as i on the nth plane jumps upward, the bonds being broken are two $\nu-1$ bonds and one ν bond. These broken bonds contribute to the $\Lambda_{\nu-2}^2$ and Λ_ν factors. The denominator is a part of the superposition relation to show that in the initial $y_\nu(i0;\ t)$ the nth lattice point is occupied by atomic species i.

The point path variables X and the pair path variables Y are defined in a similar way as in the formulation of the semiconductor superlattices. In the PPM formulation, there are no essential differences in the treatments between the infinite superlattice system and the deposited films on the semiconductor substrates. The minor difference between them is that in treating the deposited films, there are n_{s} overlayers and semi-infinite substrate in the initial state.

We choose the gradient to the <100> direction, and place the surface and deposited films above and below the substrate. In the initial state, the lattice planes for $n \le 0$ in the substrate are Si-rich and those above for $n_{\text{s}} \ge n > 0$ are Ge-rich layers. The surface is on $n\ =\ n_{\text{s}}$. The definition of the variables is the same as that in the treatment of superlattices except for $n \ge n_{\text{s}}$. We use $i\ =\ 0,\ 1,\ 2$ for a vacancy and A and B atoms. Note that, for example, in $X_n(0;\ i)_{\text{u}}$ an i atom jumps up in the downside bond. After a bit of algebra, one can get the P_3 factor of the path probability function as

$$\frac{\partial\,(N^{-1}\ln P_3\,(t,\,t+\Delta t))}{\partial Y\,(0i;\,i0;\,\nu)_{\text{d}}} = 3\left\{-\,2\ln x_n\,(0;\,t) - 2\ln x_{n+1}\,(i;\,t) + 4\ln Y\,(0i;\,i0;\,\nu)_{\text{d}}\right\} - \\ -\,2\left\{-\ln Y\,(0i;\,0i;\,\nu) + \ln Y\,(0i;\,i0;\,\nu)_{\text{d}}\right\}. \tag{18}$$

Then, summing up the terms on P_1, P_2, and $C_{\lambda\gamma}$, we obtain

$$\frac{\partial\,(N^{-1}\ln P_1\,(t,\,t+\Delta t))}{\partial Y\,(0i;\,i0;\,\nu)_{\text{d}}} + \frac{\partial\,(N^{-1}\ln P_3\,(t,\,t+\Delta t))}{\partial Y\,(0i;\,i0;\,\nu)_{\text{d}}} + \frac{\partial\,(C_{\lambda\gamma})}{\partial Y\,(0i;\,i0;\,\nu)_{\text{d}}} = 2\ln\,(\Delta t;\,\Theta_i\,(\nu)) - 6\ln x_{n+1}\,(i;\,t) + \\ +\,2\ln y_\nu\,(0i;\,t) - 2\ln Y\,(0i;\,i0;\,\nu)_{\text{d}} + 2\ln \Lambda_\nu\,({}^*i) + 4\ln \Lambda_{\nu+1}\,(i^*) = 0\,. \tag{19}$$

This leads to the final result for the exchange variable $Y(0i;\ i0;\ \nu)_{\rm d}$

$$Y\,(0i;\, i0;\, \nu)_{\rm d} = \Delta t\, \Theta_i\,(\nu)\, y_\nu\,(0i;\, t)\, \frac{\Lambda_\nu\,(^*i)\, \Lambda_{\nu+1}\,(i^*)^2}{x_{n+1}\,(i;\, t)^3}\,, \quad \nu \le n_{\rm s} - 2\,. \tag{20}$$

Using the similar transformations, we derive the result for $Y(i0;\ 0i;\ \nu)_{\rm u}$ as

$$Y\,(i0;\, 0i;\, \nu)_{\rm u} = \Delta t\, \Theta_i\,(\nu)\, y_\nu\,(0i;\, t)\, \frac{\Lambda_{\nu-1}\,(^*i)^2\, \Lambda_\nu\,(i^*)}{x_n\,(i;\, t)^3}\,, \quad \nu \le n_{\rm s} - 2\,. \tag{21}$$

From Eq. (18), we derive for $\nu = n_{\rm s} - 1$

$$\frac{\partial\,(N^{-1} \ln P_3\,(t, t+\Delta t))}{\partial Y\,(0i;\, i0;\, n_{\rm s}-1)_{\rm d}} = -\,2 \ln x\,(i;\, t;\, n_{\rm s}) - 6 \ln x\,(0;\, t;\, n_{\rm s}-1) +$$

$$+\, 2 \ln y\,(0i;\, t;\, n_{\rm s}-1) + 6 \ln Y\,(0i;\, i0;\, n_{\rm s}-1)_{\rm d}\,. \tag{22}$$

Combining Eqs. (6), (10), and (22), we obtain

$$\frac{\partial\,(N^{-1} \ln P_1\,(t, t+\Delta t))}{\partial Y\,(0i;\, i0;\, n_{\rm s}-1)_{\rm d}} + \frac{\partial\,(N^{-1} \ln P_3\,(t, t+\Delta t))}{\partial Y\,(0i;\, i0;\, n_{\rm s}-1)_{\rm d}} + \frac{\partial\,(C_{\lambda\gamma})}{\partial Y\,(0i;\, i0;\, n_{\rm s}-1)_{\rm d}} =$$

$$= 2 \ln\,(\Delta t\, \Theta_i\,(n_{\rm s}-1)) - 2 \ln x\,(i;\, t;\, n_{\rm s}) + 2 \ln y\,(0i;\, t;\, n_{\rm s}-1) - 2 \ln Y\,(0i;\, i0;\, n_{\rm s}-1)_{\rm d} + 2 \ln \Lambda\,(^*i;\, n_{\rm s}-1) = 0\,. \tag{23}$$

This leads to

$$Y\,(0i;\, i0;\, n_{\rm s}-1)_{\rm d} = \Delta t\, \Theta_i\,(n_{\rm s}-1)\, y\,(0i;\, t;\, n_{\rm s}-1)\, \frac{\Lambda\,(^*i;\, n_{\rm s}-1)}{x\,(i;\, t;\, n_{\rm s})}\,. \tag{24}$$

Compared with (20), this expression does not have the factor for the $\nu = n_{\rm s}$ bond. The equation corresponding to (21) is

$$Y\,(i0;\, 0i;\, n_{\rm s}-1)_{\rm u} = \Delta t\, \Theta_i\,(n_{\rm s}-1)\, y\,(i0;\, t;\, n_{\rm s}-1)\, \frac{\Lambda\,(^*i;\, n_{\rm s}-2)^2\, \Lambda\,(i^*;\, n_{\rm s}-1)}{x\,(i;\, t;\, n_{\rm s}-1)^3}\,. \tag{25}$$

3. RESULTS AND DISCUSSION

3a. Graphene. The discovery of carbon nanotubes with unusual geometric and electronic properties has generated considerable interest [3–7]. These tubes can be visualized as graphitic sheets rolled up into cylinders giving rise to quasi-one-dimensional structures. In the present study, the properties of carbon-related materials are investigated by using TBMD simulations. We first apply the generalized TBMD scheme to the graphite sheet. Graphite is a prototype sp^2 covalent solid, with two atoms in the unit cell and with nearest-neighbor bond length less than the sum of the covalent radii of the carbon atoms. We obtain a nearest-neighbor bond length of 1.42Å. The computed band structure is in good agreement with accepted band structure calculations. The dynamical matrix for graphite is calculated by special point averaging in the irreducible two-dimensional (2D) zone in reasonable agreement with the experimental results.

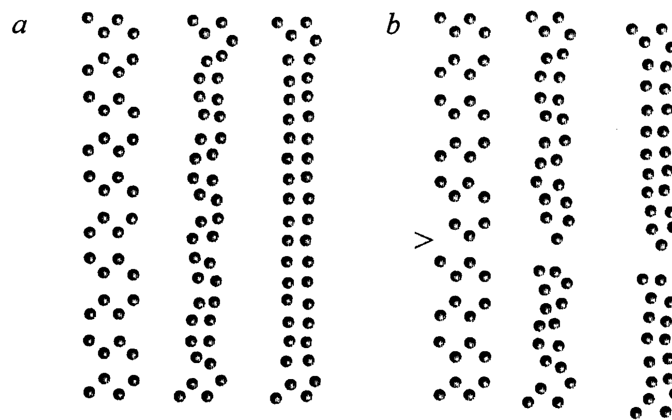

Fig. 1. Atomic configurations of quasi-1D nanowires composed of C atoms without (a) and with surface defects (b).

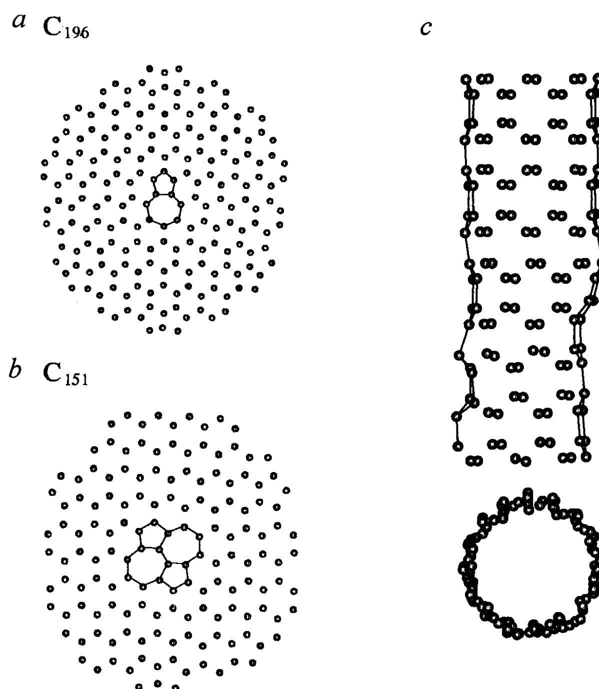

Fig. 2. 2D carbon clusters C_{196} and C_{151} including edge dislocation (a) and a pair of them (b); CNT containing *c*-axis edge dislocation (c).

In Fig. 1a, b, we present the atomic structures of quasi-one-dimensional carbon nanowires in the applied stresses, which are cut in a shape of a "belt" from graphene sheets. One can see in Fig. 1a, b that the carbon nanowires without defects show the sufficient elongation, i.e., "superplasticity" associated with the structural phase transformation like the Peierls transition of 1D system. In contrast, the carbon nanowires including surface defects like cracks (indicated by > in the figure) show very brittle fracture behavior, as shown in Fig. 1b.

We now turn to the discussion of structural defects in more realistic nanoscale materials [4-7]. In Fig. 2, we present the calculated atomic configurations of *c*-axis edge dislocation in two-dimensional planar C_{151} and C_{196} graphene clusters. The core structure of the edge dislocation is characterized by the five- and seven-membered rings in the 2D graphene sheets. In Fig. 2b, we present the atomic configurations of the pair of edge dislocations in 2D graphene clusters. The core structure of the pair of the edge dislocations is characterized by a pair of pentagon-heptagons. We have found that the pair of edge dislocations is most stable in

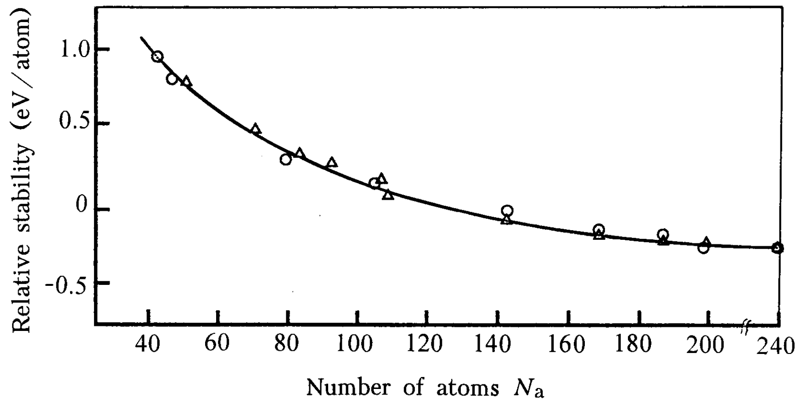

Fig. 3. Relative stabilities of carbon clusters with (△) and without (o) edge dislocations.

the configuration of Fig. 2b, and excess energies of the dislocations are further reduced for this configuration. The excess energies due to introduction of the edge dislocation are also estimated by comparing the energies of graphene sheets with and without the edge dislocations. In Fig. 3, we also show the relative stability (excess energies) of the carbon clusters as a function of the size of the clusters N_a (number of atoms). The energy is given in eV/atom units relative to that of C_{142} cluster without edge dislocations. One can see in Fig. 3 that there are no marked differences in the stability between the clusters with and without edge dislocations. This indicates that the self-energy of the edge dislocation is very small and may become even negative for certain clusters. Then, we come to the conclusion that the dislocation can be generated spontaneously without sizeable activation energy in the small semiconductor clusters. In other words, the semiconductor clusters, such as the 2D graphene clusters, can be mechanically deformed (rolled up) more easily compared to the corresponding bulk materials. The continuum elasticity theory also predicts that the elastic distortion energy of lattice defects depends on the existence of the free surfaces due to the so-called image effect [27], compared to those in the infinite crystals. However, the above-mentioned cluster-size dependence of the self-energy of the dislocation, i.e., microscopic "image effects", can not be explained within the elasticity theory.

We now describe the results of the nanoplasticity, uniaxial compression tests, of a single-wall CNT [11]. The axial compression of a CNT is achieved by keeping the edge atoms of the tube transparent to the forces generated in the GTBMD method. The positions of the edge atoms are moved axially inward at a fixed rate to compress the nanotube. As external stress is applied to nanotubes, initial linear elastic deformations are observed up to a certain critical strain beyond which nonlinear responses set in. In the nonlinear response regime, locally deformed structures such as pinches, kinks, and buckles have been observed [12]. Under the compressive stress, the nanotube exhibits the drastic change of the bonding geometry, from a graphite (sp^2) to a loca-lized diamond-like (sp^3) reconstruction, at the critical stress ($\approx$ 153 GPa). In a recent experiment, large compressive strains were applied to CNT dispersed in composite polymeric films. It has been observed that there are two distinct deformation modes, sideway buckling of thick tubes, and collapse/fracture of thin tubes without any buckling. The compressive strain in the experiment is estimated to be larger than 5%, and critical stress for inward collapse or fracture is expected to be 100–150 GPa for thin tubes.

Furthermore, it is worth noting that the simulations by the GTBMD method are significantly different from the previously reported results. For instance, the classical molecular dynamics simulations employing Tersoff–Brenner potential [5, 17] for the nanotube never plastically deform, even at larger compression. Classical molecular dynamics simulations, performed for single and multiwall CNT under tensile and compressive stresses show them to be elastic.

We also investigate the plasticity of the single-wall carbon nanotube containing dislocations, whose core is characterized by the pentagon-heptagon pairs. In Fig. 2c, we present the atomic structure of carbon

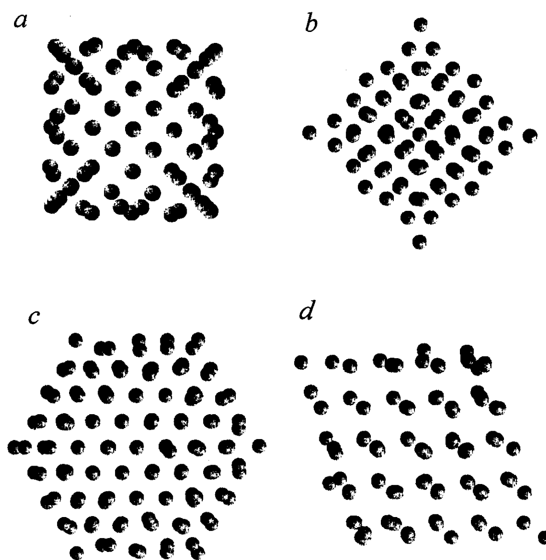

Fig. 4. Atomic configurations of Si_{95} (a), Si_{76} (b), and Si_{165} (c and d)

nanotube containing the edge dislocation. One can see in Fig. 2c that a stepwise change of a diameter appears near the dislocation. We have found that the CNT containing the edge dislocation exhibits the critical stress far below (~80 GPa) than that (153 GPa) of the CNT without dislocation. The *c*-axis edge dislocation provides the efficient center for stress concentration and gives rise to the failure of the CNT. The details of the plastic flow and failure depend on the symmetry of CNT and will be presented elsewhere.

3b. Nanocrystalline Si. Semiconductor nanoclusters are crystallites of semiconductor material with diameters between 10 and 100Å. Their atomic structure is similar to that of bulk semiconductor as shown by x-ray studies and electron microscopy. The optical and electronic properties differ markedly from the bulk and are strongly size-dependent [28–31]. The size-dependence is evident in the increase in the fundamental band gap and first absorption energy as the cluster size is decreased. The electronic and optical properties of nanoclusters are explained qualitatively by assuming that the electrons and holes are confined within the nanocluster, known as "quantum size" effect [28–31].

So far, the atomic and electronic structures of Si clusters have been extensively studied for smaller clusters ~Si_{20}, but little is known about the atomic structures and the related physical properties of the larger clusters. For instance, Si_{45} has attracted a lot of attention due to its experimentally known low reactivity to several molecules compared to most stable silicon surfaces [32]. Five different theoretical models of Si_{45} (I–V) have been proposed by Kaxiras (I) [33], Pan and Ramakrishna (II) [34], Patterson and Messmer (III) [35], Jelski et al. (IV) [36], and Rothlisberger (V) [37]. The Si_{45} cluster found by Rothlisberger et al. using the Car-Parinello method has 12 dangling bonds and lowest energy among the five structures [37]. Using the present GTBMD, we have checked that the Si_{45} cluster of model V is the most stable. However, the definite conclusion on the relative stability of Si_{45} cluster has not been given yet.

In Fig. 4, we show the atomic configurations of nanoscale Si_{95}, Si_{76} and Si_{165} clusters. The initial structure of a Si_{95} cluster is cubic shaped and (001) faceted, i.e., all surfaces are covered with (001) surfaces, while those of Si_{76} and Si_{165} clusters are (111) faceted. i.e., covered by (111) surfaces. In the relaxed configurations, all of these Si clusters retain the symmetry of the initial unrelaxed cluster structures. One can see that there are volume shrinkage of the order of ~20% for the Si clusters and the tendency is stronger for the smaller Si crystallites.

We have also investigated the core properties of dislocations in the nanoscale Si crystallites. The properties of dislocations in Si clusters are also different from those of the bulk crystals. In a diamond cubic crystal, the important dislocations are the 60°, screw, and 90° (edge) perfect dislocations [27]. The first one

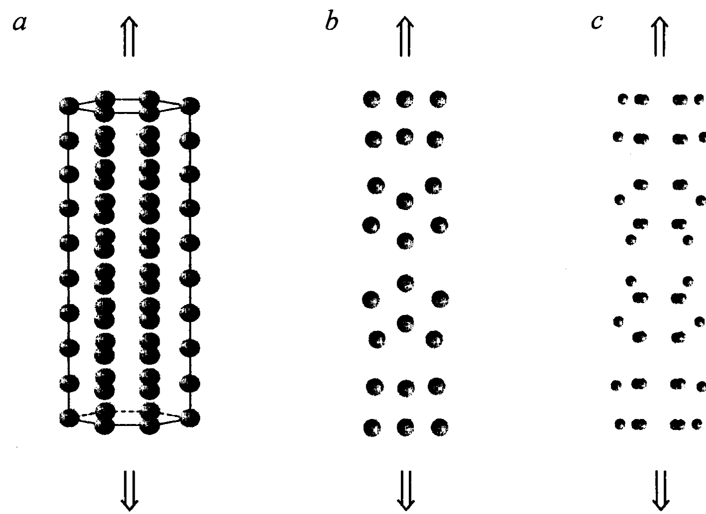

Fig. 5. Tensile tests of $(Si_6)_n$ nanowires: unstrained nanotube (a) and strained structures (b and c, with c being rotated by 90° with respect to b).

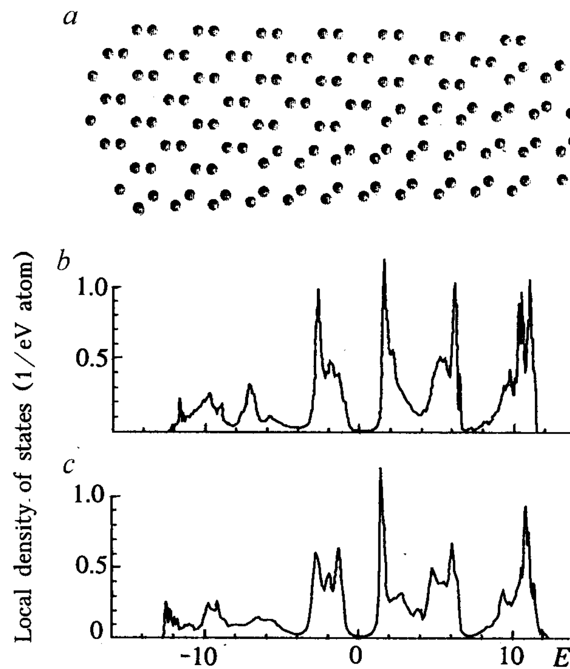

Fig. 6. Atomic geometry of Si nanowire including Σ = 9 (221) tilt grain boundary (a); local electronic DOS of Si quantum wires without (b) and with (c) Σ = 9 (221) grain boundaries. *E*, eV.

dissociates into 30° and 90° partial dislocations while the others split into a pair of 30° and 60° partial dislocations, respectively. All the partials are separated by intrinsic stacking faults. These partials which have line directions along <110> are believed to be reconstructed into a structure with no dangling bonds. The atomic configurations of 30° partial dislocations in Si_{150} and in a bulk Si crystal are compared, and it has been found that the reconstruction defect "solitons" can be seen near the center of the Si_{150} crystallite [13]. These point singularity "solitons" in the small crystallites are formed by the atomic reconstruction, which are initiated from the crystallite surface. Therefore, they are different in nature from those appearing along the dislocation line in the bulk crystal, which are thermodynamic reconstruction defects.

In addition, we consider the factious Si nanowires composed of six-membered Si rings $(Si_6)_n$ as shown in Fig. 5, whose initial structure is suggested from the structure of type IV Si_{45} cluster. Under the tensile stress, this type of nanowire exhibits the nonuniform deformation, and certain necking occurs near the center region of the nanowire. The appearance and location of the necking depend sensitively on the size of the wire, and we have found that the necking occurs near the edge of wires for larger sizes.

We have also considered more realistic Si quantum wires with extended defects. This is simply because that the Si quantum wires synthesized by laser ablation often contain the kinks, twins, and grain boundaries [39]. It is also known that the quality of the polycrystalline Si films depends on their texture [40] because the tilt grain boundaries are generally believed to be electrically inactive. Therefore, it is of great significance to investigate the atomistic and electronic structures of dislocations and grain boundaries in microcrystalline semiconductors.

To calculate the electronic density of states (DOS) of nanocrystalline Si, we use the Chebychev moment method [38]. We consider the calculation of the DOS of an $N \times N$ Hamiltonian $\mathbf{H}$, with eigenenergies ε_n. In Fig. 6, we present the calculated atomic configuration (a) and electronic DOS of the Si nanowires, without and with the $\Sigma = 9$ (221) tilt grain boundaries (b, c). One can see in Fig. 6 that for the quantum wire with square $(110) \times (\bar{1}10)$ cross sections of a 10×10 monolayer, the band gap region becomes wider due to the quantum size effects compared to that of the bulk Si crystal. It can also be seen that the $\Sigma = 9$ (221) tilt grain boundary GB does not produce the prominent gap states. The similar conclusion of the non-appearance of gap states is also reported for the tilt grain boundaries in bulk Si crystals.

3c. Semiconductor Heterostructure. Before going into the details of the PPM, we first estimate the effective pair interaction energies between the constituent atoms in the system. The effective pair interaction energies are very important quantities in discussing the thermodynamic stability of the alloy systems. For instance, it is known that crystalline $Si_{1-x}Ge_x$ mixture is a random alloy at room temperature, and this mixture phase separates into Si-rich and Ge-rich phases below the critical temperature $170 < T_c < 240$ K [19]. It is important (but difficult) to investigate whether the tendency for phase transition is increased or decreased in the strained superlattice or in the strained overlayers. Recently, it has been pointed out that the amorphous network of a Si–Ge mixture, under thermodynamic equilibrium, does not phase separate. In the present study, we investigate the segregation behavior in the semiconductor heterojunction by calculating the ordering energy ε $[= \varepsilon_{AA} + \varepsilon_{BB} - 2\varepsilon_{AB}]$ between the constituent atoms, using the tight-binding electronic theory and orbital peeling method [41–45].

To calculate the lattice relaxation around solute atom, we use the TB scheme proposed by Li and Myles [46]. According to their TB scheme, the diagonal-matrix elements are taken to be proportional to the atomic energy differences of the impurity atom and the replaced host atom

$$\Delta\upsilon_{II} = \beta_i\,(\varepsilon_I^i - \varepsilon_H^i)\,,$$

where $i = s$ and p, ε_I^i and ε_H^i are the atomic energies of the impurity atom and the host atom for orbital i; the proportional factors are taken to be $\beta_s = 0.8$ and $\beta_p = 0.6$. The off-diagonal matrix elements of the defect potential is based upon Harrison's scheme for the nearest-neighbour transfer-matrix elements of the host Hamiltonian. They are scaled as the inverse of the bond length squared. We assume that the same scaling rule holds for the transfer-matrix elements of both the solute containing and the perfect crystals. Since the off-diagonal matrix elements of the defect potential are differences in such transfer matrix elements, this allows them to be written as

$$\Delta\upsilon_{IH} = -\,C_i\,[(d_I)^{-2} - (d_H)^{-2}]\,.$$

We also take into account the modification of the scaling laws of the TB parameters at the strained overlayers [47–49].

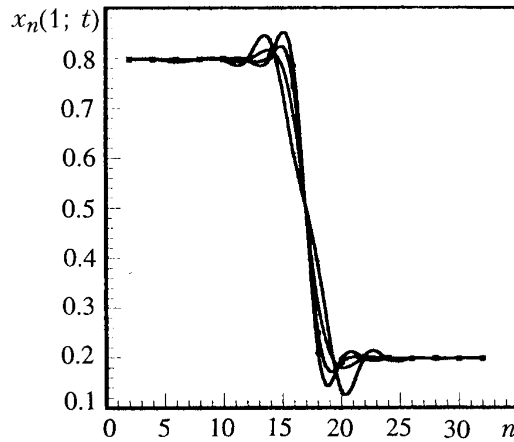

Fig. 7. Relaxation of composition profile (diamond cubic structure) obtained by integration with the initial composition of $x_n(1) = 0.2$ at the flat bottom and 0.8 at the flat top for different time steps from 5000 to 60,000 in an arbitrary time interval.

The change in the band structure energies ΔF due to introduction of the local perturbation (point defect) is calculated from the following formula

$$\Delta F = \int^{E_F} (E - E_F)\,\Delta\rho\,(E)\,dE = -\sum_{il} Z_{il} + \sum_{il} P_{il} - (N_P - N_Z)\,E_F + \sum_{il} Z_{il}^0 - \\ - \sum_{il} P_{il}^0 + (N_P^0 - N_Z^0)\,E_F\,,$$

where $Z_{il}(Z_{il}^0)$ and $P_{il}(P_{il}^0)$ are the zeros and poles of the Green's function corresponding to a recursion starting from a coordination sphere $i + 1$ as if the previous coordination spheres were absent. N_Z (or N_Z^0) and N_P (or N_P^0) are the total numbers of zeros and poles of the crystal including the local perturbation (or without it). We perform the calculations of ΔF for single impurity as well as for a pair of the impurities and derive the pair interaction energies between them.

The ordering energies of Si_xGe_{1-x} mixture are calculated to be 19 meV and 35 meV for the unrelaxed and relaxed atomic configurations, respectively. The order of magnitude of these ε values may be compared with the enthalpy of formation ΔH(a-$Si_{1-x}Ge_x$) = –14 meV/atom ($x = 0.5$) for the amorphous *a*-SiGe alloy at 100 K calculated by Tzoumanelas and Kelires [19].

Using the effective pair interaction energies derived by the TB orbital peeling method and the PPM for the interface relaxation, we have performed some calculations on the interface disorder of SiGe/Si(001) system. The relaxations of the semiconductor heterojunctions are investigated for both the superlattice structures and the deposited films on the substrate. In Fig. 7, we present the calculated profiles of semiconductor heterojunction with diamond cubic (001) interfaces using the effective interaction energies appropriate for the SiGe/Si(001) systems. We made the general assumptions that the jump probabilities of species A (Si) and B (Ge) are the same, and made $\varepsilon_{AA} = \varepsilon_{BB}$, where ε_{ij} is defined as the energy needed to break an i–j bond. In the TB orbital peeling method, we obtained $4\varepsilon = \varepsilon_{AA} + \varepsilon_{BB} - 2\varepsilon_{AB} > 0$ for SiGe/Si(001) system. This implies that A(Si-rich) and B (Ge-rich) phases separate at low temperatures. Taking into account the critical temperature of phase separation, we choose $2\varepsilon/kT = 0.12$ for the present calculation so that the equilibrium profile is uniform throughout the system. In Fig. 8, we also present the calculated profiles of the superlattice struc-

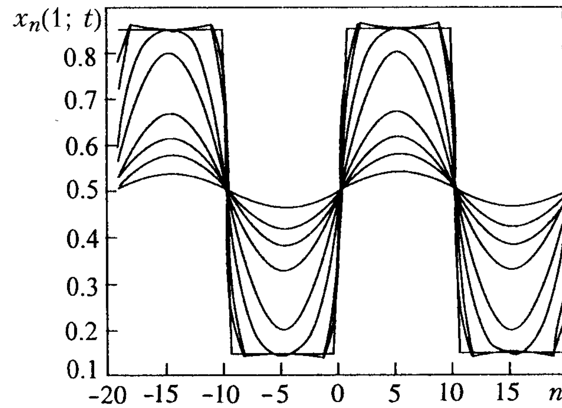

Fig. 8. Relaxation of composition profile (fcc structure) obtained by integration with the initial composition of $x_n(1) = 0.15$ at the flat bottom and 0.85 at the flat top for different time steps from 450 to 150,000 in an arbitrary time interval.

tures with fcc(001) interfaces. For this system, we choose $2\varepsilon/kT = 0.15$, indicating also that the equilibrium profile is uniform throughout the system.

Summarizing the example calculations of the relaxation of semiconductor heterojunctions, we have found the following characteristic features:

(i) At the initial stage of relaxation of a sharp profile, overshooting of the profile occurs.

(ii) Near a sharp junction profile, the atom flux changes sign during relaxation.

(iii) Near the junction, the chemical potential gradient becomes zero at a time t^* different from that of the atom flux. There is a time period in which atoms do not flow downhill along the chemical potential gradient.

(iv) The local chemical potential gradient in a nonequilibrium state depends not only on the density gradient but also on atomic pair correlation.

(v) While the overshooting is occurring, the free energy of the entire system monotonically decreases.

(vi) The overshooting can be understood by a kinetic reasoning as due to the repulsion of atoms.

Furthermore, we have also found that the interface disorder influences quite significantly the electronic and optical properties of the semiconductor heterostrucutres. Even for the very early stage of the junction relaxation, i.e., after ~100 time steps, the electronic states of the heterojunction are influenced significantly by the interface disorder compared with those of the sharp interface. We have found that when one of the atoms in the core of the misfit dislocations (both 1/2 <001> (001) edge type and 60° shuffle set dislocation) in GaAs/ZnSe(001) system is changed by interface mixing, the dislocation induced gap state is drastically altered, it even leads to the disappearance of the gap states [21]. This indicates that the appearance of electronic bound states of the misfit dislocations must be calculated on the basis of the precise atomic geometries in the core region of the misfit dislocations.

We now briefly summarize the calculations of the present subsection. We have studied the semiconductor heterostructures with ideal interfaces as well as those with interface disorder. The atomic disorder at the interface is investigated using a vacancy mechanism of diffusion. The PPM is formulated for the two types of the semiconductor heterostructures, the semiconductor superlattices and deposited films on the semiconductor substrates. For the relaxation process, it has been suggested that the large and measurable interlayer mixing occurs at the Ge/Si(001) heterojunction at the initial stage of the relaxation. For heterojunctions like GaAs/AlAs(001) we allow cationic intermixing, which very likely takes place during the growth process. For treating the interdiffusion in the (001) direction of zincblende structure, we simply take one of the sublattices. We have found that the interface disorder influences quite significantly the electronic properties of the semi-

conductor heterostructures. The present atomistic simulation is also of significance, as a first stage, to treat more general junction geometries like (113) heterostructures.

4. CONCLUSIONS

We have studied the atomistic and mechanical properties of nanoscale semiconductor crystallites, using the O(N) TBMD method. This method is very efficient and reliable scheme to study properties of large scale systems. The properties of extended dislocations like dislocations and grain boundaries in nanoscale materials depend sensitively on the size of the crystallites and differ significantly from those of the bulk materials, especially in semiconductor clusters due to the nanoscale "image effects". It has also been found that the edge dislocation whose core is characterized by pentagon-heptagon pair acts as the center for the stress concentration and contribute to the plastic deformation far below the stress level than the critical stress of CNT including no defects.

In the present study, we have also considered semiconductor (001) heterostructures with ideal interfaces as well as those with interface disorder. For heterojunctions like GaAs/AlAs and ZnSe/GaAs, we allow cationic intermixing, which very likely takes place during the growth process. For treating the interdiffusion in the (001) direction of zincblende structure, we use a vacancy mechanism of diffusion and simply takes one of the sublattices. We have found that the interface disorder influences quite significantly the electronic properties of the semiconductor heterostrucutres. The present atomistic simulation is also of significance, as a first stage, to treat more general junction geometries like (113) heterostructures.

NOTATION

U, total energy of the system; ε_k, band structure energy of *k*th occupied state; *t*, time; ϕ, repulsive potential; r_{ij}, separation between atoms *i* and *j*; *P*, path probability function; *N*, number of lattice points; *n*, plane position; θ_i, oscillation frequency of *i*th atom; ε_{ij}, pair energy; *a*, lattice constant; N_a, number of atoms; *F*, band structure energy. Subscripts: el, electron; rep, repulsive; u, upward jump of an atom; d, downward jump of an atom; pt, point; I, impurity; H, host.

REFERENCES

1. H. W. Kroto, J. R. Heath, S. C. O'Brien, R. F. Curl, and R. E. Smally, *Nature*, **318**, 162 (1985).
2. W. Kratschmer, L. D. Lamb, K. Fostiropoulos, and D. R. Huffman, *Nature*, **347**, 354 (1990).
3. S. Iijima, *Nature*, **354**, 56 (1991).
4. A. J. Stone and D. J. Wales, *Chem. Phys. Lett.*, **128**, 501 (1986).
5. D. W. Brenner, *Phys. Rev.*, **B42**, 9458 (1990).
6. B. I. Yakobson, *Appl. Phys. Lett.*, **72**, 918 (1998).
7. B. I. Yakobson, C. J. Brabec, and J. Bernholc, *Phys. Rev. Lett.*, **76**, 2511 (1996).
8. M. Menon and K. R. Subbaswamy, *Phys. Rev.*, **B50**, 11577 (1994).
9. M. Menon, E. Richerter, and K. R. Subbaswamy, *J. Chem. Phys.*, **104**, 5875 (1996).
10. M. Menon and K. R. Subbaswamy, *Phys. Rev.*, **B55**, 9231 (1997).
11. D. Srivastava, M. Menon, and K. Cho, *Phys. Rev. Lett.*, **83**, 2973 (1999).
12. O. Lourie, D. M. Cox, and H. D. Wagner, *Phys. Rev. Lett.*, **81**, 1638 (1998).
13. K. Masuda-Jindo, M. Menon, K. R. Subbaswamy, and M. Aoki, *Comp. Mat. Sci.*, **14**, 203 (1999).
14. S. C. Jain, J. R. Willis, and R. Bullough, *Adv. Phys.*, **39**, 127 (1990).
15. R. Beanland, D. J. Dunstan, and P. J. Goodhew, *Adv. Phys.*, **45**, 87 (1996).
16. B. Voigtländer and M. Kastner, *Phys. Rev.*, **B60**, R5121 (1999).

17. J. Tersoff, *Phys. Rev.*, **B45**, 8833 (1992).
18. Ch. Ratsh and A. Zaugwill, *Surf. Sci.*, **293**, 123 (1993).
19. C. Tzoumanekas and P. C. Kelires, *J. Non-Cryst. Solids*, **266–269**, 670 (2000).
20. W. Bala, M. Drozdowski and M. Kozielski, *Phys. Stat. Sol.*, **130a**, K195 (1992).
21. K. Masuda-Jindo, *Microstructures and Superlattices*, **20**, 117 (1996).
22. B. K. Rai and R. S. Katiyar, *J. Appl. Phys.*, **83**, 6011 (1998).
23. R. Kikuchi, *Prog. Theor. Phys. Suppl.*, **35**, 1 (1966).
24. R. Kikuchi and H. Sato, *J. Chem. Phys.*, **53**, 2702 (1970).
25. R. Kikuchi and K. Masuda-Jindo, *Comp. Mat. Sci.*, **14**, 295 (1999).
26. R. W. Nunes and D. Vanderbilt, *Phys. Rev.*, **B50**, 17611 (1994).
27. J. P. Hirth and J. Lothe, *Theory of Dislocations,* McGraw-Hill, New York (1968).
28. S. Y. Ren and J. D. Dow, *Phys. Rev.*, **B45**, 6492 (1992).
29. Chin-Yu Yeh, S. B. Zhang, and A. Zunger, *Phys. Rev.*, **B50**, 14405 (1994).
30. M. Lannoo, C. Delerue, and G. Allan, *Phys. Rev. Lett.*, **74**, 3415 (1995).
31. A. Zunger and L.-W. Wang, *Appl. Surf. Sci.*, **102**, 350 (1996).
32. Th. Frauenhein, F. Weich, Th. Kohler, S. Uhlman, D. Porezag, and G. Seifert, *Phys. Rev.*, **B52**, 11492 (1995).
33. E. Kaxiras, *Phys. Rev. Lett.*, **64**, 551 (1990).
34. J. Pan and M. V. Ramakrishna (unpublished).
35. C. H. Patterson and R. P. Messmer, *Phys. Rev.*, **B42**, 7530 (1990).
36. D. A. Jelski et al., *J. Chem Phys.*, **95**, 8552 (1991).
37. U. Röthlisberger, W. Andreoni, and M. Parrinello, *Phys. Rev. Lett.*, **72**, 665 (1994).
38. A. F. Voter, J. D. Kress, and R. N. Silver, *Phys. Rev.*, **B53**, 12733 (1996).
39. N. Wang, Y. H. Tang, Y. F. Zhang, D. P. Yu, C. S. Lee, I. Bello, and S. T. Lee, *Chem. Phys. Lett.*, **283**, 368 (1998).
40. G. Wagner, H. Wawra, W. Dorsch, M. Albrecht, R. Krome, H. P. Strunk, S. Riedel, H. J. Moller, and W. Appel, *J. Cryst. Growth*, **174**, 680 (1997).
41. F. Wu and M. G. Lagally, *Phys. Rev. Lett.*, **75**, 2534 (1995).
42. B. Voigtländer and A. Zinner, *Appl. Phys. Lett.*, **63**, 3055 (1993); B. Voigtländer, A. Zinner, and Th. Weber, *Rev. Sci. Instrum.*, **67**, 2568 (1996).
43. N. R. Burke, *Surf. Sci.*, **58**, 349 (1976).
44. P. J. Lin Chung and T. L. Reineke, *Phys. Rev.*, **B27**, 1101 (1983).
45. C. Wolverton, D. de Fontaine, and H. Dreysse, *Phys. Rev.*, **B48**, 5766 (1993).
46. W. G. Li and C. W. Myles, *Phys. Rev.*, **B43**, 2192 (1991).
47. S. Y. Ren, J. D. Dow, and D. J. Wolford, *Phys. Rev.*, **B25**, 7661 (1982).
48. C. Priester, G. Allan, and M. Lannoo, *Phys. Rev.*, **B38**, 9870 (1988).
49. Q. M. Ma, K. L. Wang, and J. N. Schulman, *Phys. Rev.*, **B47**, 1936 (1993).